Defocusing PTV applied to an open wet clutch – from macro to micro

R. Leister[1,*], T. Fuchs[2], J. Kriegseis[1]

1: Institute of Fluids Mechanics (ISTM), Karlsruhe Institute of Technology, Germany
2: Institute of Fluid Mechanics and Aerodynamics, Universität der Bundeswehr München, Germany
*Corresponding author: robin.leister@kit.edu

Keywords: Defocusing PTV, Micro flows, open wet clutch

ABSTRACT

The approach of defocusing particle tracking velocimetry (defocusing PTV) is applied in various levels of magnification to the fluid flow of an open wet clutch with radial grooving. The magnification ranges from $M = 0.8$ up to $M = 15$, whereas corresponding defocusing sensitivities ranges from 67.1 to 9.0 µm/pixel. This specific set-up appears necessary, since a comparative wide field-of-view as well as a detailed consideration inside the groove seems equally important for this particular scenario. It can be shown that all optical configurations can properly depict the occurring fluid flow phenomena that are present in an open wet clutch. The smallest magnification can properly depict the region between the inner and the outer radius and is thus closing the academic gap for open clutch flows, since a groove-to-groove analysis as well as an evaluation along the entire radius becomes possible. The smallest magnification yields the highest accuracy in terms of {x,y} and also in z-direction. The accuracy in z-direction is quantified with the region near to the stator, where the theoretical axial velocity should be zero. The set-up with $M = 0.8$ reaches an uncertainty of the particle-image diameter of $2\sigma_{d_\mathrm{i}} = 0.24$ pixel. The remaining set-ups have higher uncertainties. The smaller defocusing sensitivity cannot outperform the loss in intensity and a less distinct intensity peak at the outer part of the defocused image due to the large magnification and the used *Questar* lens. These findings are supported by a fluid flow analysis, where the circumferential velocity u_φ in the middle of the groove is used as comparative case. All magnifications were able, to depict the considered velocity properly, while the uncertainty increases for higher-magnification configurations. In summary, the present study demonstrates the feasibility and robustness of the defocusing PTV-approach for such sub-millimeter gap-flow scenarios in technical applications. The flexibility in terms of magnification reached within this experimental investigation makes defocusing PTV a candidating technique for such industry-relevant research scenarios.

1. Introduction

The continuous development of new hybrid and battery-driven drive concepts in automotive industry, forced by the desire to save CO_2 emissions, led to a large variety of new energy-saving

strategies. One of the strategies is the optimization of idling behavior of a wet clutch, which is presently installed in the majority of higher-class automobiles. The speed difference between drive and output, the sub-millimeter gap height, and the presence of oil between the disks result in a considerably high wall-shear stress, which sums up to an adverse so-called *drag torque*. A vast amount of research and development efforts addressed the minimization of this adverse torque, which mostly led to a variety of different groove patterns on one of the disk groups in the clutch packages. A variety of different investigations were conducted to clarify the influence of these patterns on the basis of torque measurements (Neupert et al., 2018; Grötsch et al., 2019).

However, a precise experimental investigation of the cause-effect relations between disk geometry and resulting adverse drag torque has ever since been considered rather difficult, due to the limited availability of apt measurement techniques. When using an estimate to quantify the ongoing phenomena in the sub-millimeter gap the use of an integral measurement method inherently leads to the loss of information and renders a precise inter-dependency rather difficult. This scenario is in need of an appropriate measurement technique, that meets all mandatory side conditions and persists the fairly rough environment with complex geometries and accordingly high amount of reflection when investigated with laser-based velocimetry, for instance. As already shown by Leister, Fuchs, et al. (2021), the technique of Defocusing Particle Tracking Velocimetry (defocusing PTV) is able to extract the complete 3D3C velocity information within a radially-grooved open wet clutch, as well as the resulting wall-shear-stress (WSS) on the stator.

For the present clutch flow study, different optical configurations with changing magnifications - from macroscopic to microscopic - were used, in order to resolve different levels of detail. Thus, an overview measurement was conducted with a relatively small magnification, capturing the in- and outflow of the clutch gap. Configurations with a larger magnification focused on the measurement of the more complex flow structures in the vicinity of the groove. The significant effect of these flow patterns in the groove domain on the overall flow field were already highlighted by (Leister, Fuchs, et al., 2021). With the investigations presented here, a comparative analysis of different levels of magnification for the fluid flow at hand was conducted. Furthermore, a comparative assessment of different optical configurations helps to select the appropriate set-up for a given measurement task.

2. Defocusing PTV

2.1. Measurement principle

In general, defocusing of particle images uses the additional information of a certain out-of-focus behavior and, since its introduction by Willert & Gharib (1992), proved popularity as macroscopic, but even more as microscopic measurement technique. The theoretical mathematical description of the particle image d_i under absence of optical aberrations is a sum of the geometric image, the diameter change due to diffraction and the defocusing term. These relationships had been

summarized by Olsen & Adrian (2000) and can be written as

$$d_{\mathrm{i}}{}^2 = \underbrace{M^2\, d_{\mathrm{p}}{}^2}_{\text{geometric image}} + \underbrace{5.95\,(M+1)^2\,\lambda^2 f_{\#}^2}_{\text{diffraction}} + \underbrace{\frac{M^2 z^{*2} D_{\mathrm{a}}{}^2}{(s_0+z^*)^2}}_{\text{defocusing}}\,. \tag{1}$$

Here, M appears as magnification, d_{p} as physical particle diameter, λ as wave length of the emitted light and $f_{\#}$ is the focal number of the lens. The third term is modeling the defocusing principles and describes the diameter change of the particle on the image plane as function of the distance z^* between the particle and the focal plane, the distance s_0 between the lens and the focal plane and the physical diameter of the used aperture D_{a}. For practical defocusing this equation can be simplified further. For normal imaging application $s_0 \gg z^*$ applies for any optical set-up such that the image-diameter change can be approximated by

$$d_{\mathrm{i}}(z^*) \propto \left(\text{const.} + z^{*2}\right)^{1/2}. \tag{2}$$

This hyperbola can be approximated as linear interdependency when considering out-of-focus elements that have a sufficient distance to the focal plane. Equation (2) can thus be simplified to

$$d_{\mathrm{i}}(z^*) \propto z^*. \tag{3}$$

Since each commercial lens has correcting-glass elements for minimizing a vast array of aberrations (e.g. field curvature, spherical aberration, chromatic aberration), the exact intensity distribution - and thus diameter - relies on the lens and various further factors. A direct implementation of Equation (1) would lead to unacceptably strong deviations and errors of the position estimation. However, this theoretical consideration might lead to a first estimate and paves the ground for a justified overall approach. A partial derivation of Equation (1) in regard to z^* leads to a theoretical defocusing sensitivity δ_{s}. This dimensionless value appears as theoretical quality factor and can be used for defocusing approaches in general. A formulation of this value can be stated as

$$\delta_{\mathrm{s}} = \frac{\partial d_{\mathrm{i}}}{\partial z^*} = \frac{M D_{\mathrm{a}}}{s_0}\left(= \frac{s^{XY}}{s^Z}\right). \tag{4}$$

To overcome the void between the theoretical consideration and the desire to extract meaningful results, the present study uses the *in situ* calibration approach of Fuchs et al. (2016), where the extracted diameter is locally transformed in physical units on the basis of known boundary conditions in terms of particle displacements. The introduced theoretical defocusing sensitivity δ_{s} can also be expressed with help of the reproduction scale s^{XY} and the dimensional defocusing sensitivity s^Z.

2.2. Experimental set-up

An overview of the experimental set-up is given in Figure 1 on the left, while a more detailed view of the clutch geometry is shown on the right. The stator is made from glass with a thickness of 3 mm to allow an optical access for viewing and illuminating the clutch gap. The rotor is

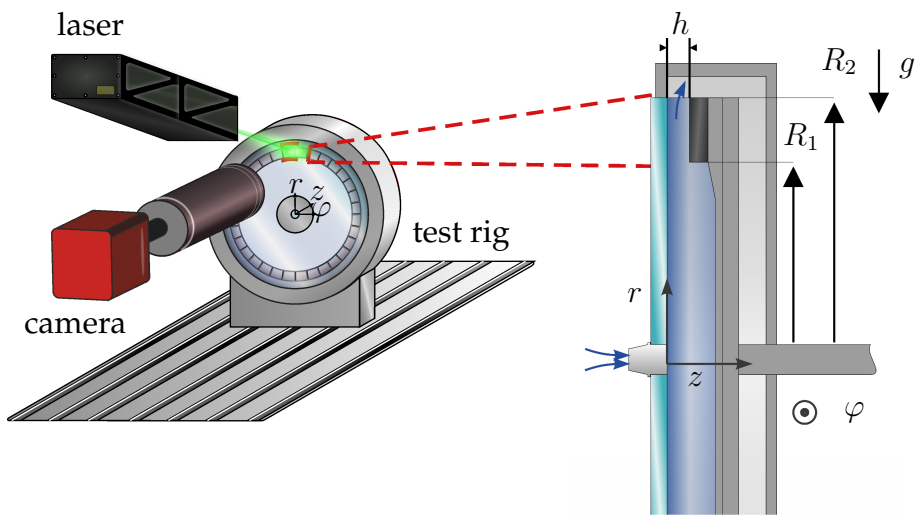

Figure 1. Sketch of the experimental set-up (left) and the test rig (center) for the conducted defocusing PTV experiments.

made from aluminum, whereas exchangeable polymer clutch disks can be added depending on preference. The disks are manufactured by 3d printing (*Formlabs Form 3L*, layer thickness 50 µm), to allow for complex geometries and fine details of the groove patterns. The clutch geometry is characterized by the following parameters: (1) the inner radius $R_1 = 82.5$ mm; (2) the outer radius $R_2 = 93.75$ mm; (3) the gap height $h = 400$ µm between the clutch surface and the stator; (4) in case of the radially grooved clutch: the groove parameters, which are the width of $W = 1.35$ mm at the groove bottom, the groove height of $H = 1.0$ mm, and the pitch between the grooves of $11.25\,^\circ$ along the perimeter. To suppress light reflections on the clutch surface, fluorescent melamine resin based seeding particles with a mean diameter of $d_\mathrm{p} = 9.84$ µm were used to seed the white mineral oil (CAS No: 8042-47-5, $\rho_0 = 850\,\mathrm{kg/m^3}$, $\nu = 16 \times 10^{-6}\,\mathrm{m^2/s}$), which is supplying the clutch. The seeding particles, emitting a wave length of $\lambda_\mathrm{em} = 584$ nm and were excited at a wave length of $\lambda = 532$ nm with a double-pulsed *Quantel Evergreen* Nd:YAG laser (210 mJ). A band pass filter ($\lambda = 590 \pm 10$ nm) was placed between the camera sensor and the measurement domain, to only capture the fluorescent light of the particles.

To investigate different optical configurations, the *pco.edge 5.5* sCMOS camera was equipped with a variety of objective lens combinations, including a *Zeiss Makro-Planar* $f = 50$ mm and a *Questar QM 1* telescope, which is further referred to as a long-distance microscope. A detailed analysis of the optical characteristics of the lens combinations is outlined in the following.

2.3. Optical characteristics

Depending on the required spatial resolution, the optical set-up can be adapted in terms of varying magnifications. However, changing the optics in turn changes the imaging characteristics. Therefore, certain key parameters are assessed that characterize a defocusing PTV set-up in this section, including the magnification M, the reproduction scale s^{XY}, the FOV size, and the defocusing sen-

sitivity s^Z. The latter parameter denotes the relation between the change of the particle-image diameter over the particle z location, i.e. along the optical axis. In principle, this means that a stronger change of the particle-image diameter over a certain z distance means that the particle z location can be determined more accurately.

Altogether four different magnifications were investigated, where the first configuration with the smallest M comprised a *Zeiss Makro-Planar* $f = 50$ mm at the shortest possible working distance together with a 20 mm distance ring to yield the largest possible magnification, which was still capturing the entire radial extent of the clutch gap. An overview of the parameters of all optical configurations is given in Table 1, while Figure 2 illustrates the FOV extent in comparison to the clutch geometry. The three larger-magnified configurations comprised a *Questar QM 1* long-distance microscope as imaging optics, which was positioned at shortest possible distance of 56 cm. Here, the magnification was adjusted by adding magnifying lenses between the camera and the lens. Note that the FOV size for the *Zeiss* 50 mm configuration was cropped due to optical distortions in the image corners, whereas for the *Questar* configurations the entire sensor was used.

In terms of the accuracy of the particle z-location determination, the defocusing sensitivity s^Z, listed in the last column of Table 1, is a decisive factor. With increasing magnification s^Z decreases, meaning with a certain change of the particle z location, the particle-image diameter increases/decreases by a larger amount. However, it becomes apparent that s^Z does not scale linearly with M, since for the first two set-ups (*Zeiss* 50 mm and *Questar* + $2\times$), the M ratio yields around 6, while s^Z ratio yields around 3 (cp. first two rows in Table 1). This is due to the fact that with different lens configurations quantities such as the aperture diameter, D_a, change. As can be seen from Equation (1), D_a changes the slope of the relation between z and the particle-image diameter. Considering only at the *Questar* configurations, also *Questar* + $6\times$ does not scale linearly with the magnification. The reason for this is the addition of magififying lenses, which actually changes the largest opening diameter of the light path D_a. The subsequent section addresses the accuracy of the particle z location in relation to the defocusing sensitivity s^Z and classifies the results in the current literature.

Table 1. Optical parameters for the different optical configurations, where s^{XY} denotes the reproduction scale and s^Z the defocusing sensitivity.

configuration	M [-]	FOV [mm^2]	s^{XY} [µm/pixel]	s^Z [µm/pixel]
● *Zeiss* 50 mm	0.8	12×12	7.57	67.1
● *Questar* + $2\times$	5.2	3.2×2.7	1.25	23.4
● *Questar* + $3\times$	7.6	2.2×1.8	0.86	15.5
● *Questar* + $6\times$	15	1.1×0.9	0.43	9.0

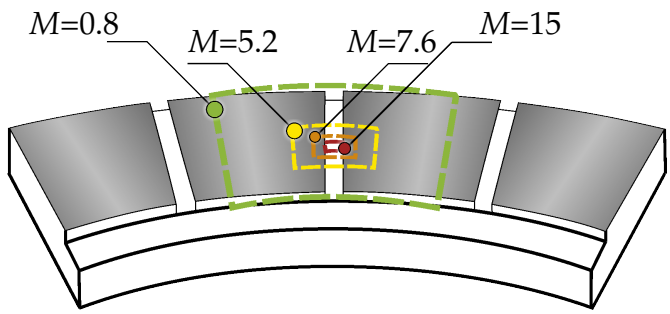

Figure 2. Overview of the FOV locations and the corresponding magnifications, M, for all the optical configurations listed in the first column of Table 1.

3. Results

3.1. Particle location uncertainty

As already generally outlined from a theoretical perspective in Section 2.1, a stronger rate of change of the particle-image diameter over the particle z location, i.e. along the optical axis, yields an increased resolution. That is, from a theoretical point of view, higher magnifications, which leads to lower s^Z-values as already shown in Table 1, might have a lower uncertainty of the particle location.

However, changing the optical configuration also changes the imaging characteristics and, therefore, the appearance of the particle images. Thus, the intensity distribution of the particle images change and with this the signal-to-noise ratio (SNR), among other factors. For the optical configurations presented in this study, the relation between s^Z and the uncertainty of the particle z location determination are assessed in the following to find whether the theoretical consideration is meaningful.

To do so, the assumption that the velocity component u_z is close to zero in the vicinity of the stator is made, which is justified as shown by Leister, Fuchs, et al. (2021). Due to the measurement uncertainty, for a single particle track a non-zero u_z velocity is estimated, such that the standard deviation of the velocity component in z direction can be calculated and transferred into a location uncertainty σ_z (in µm), and an uncertainty of the particle-image diameter σ_{d_i} (in pixel). This standard deviation is a measure of the uncertainty of the particle-image diameter determination, which effectively denotes the uncertainty of the particle z location determination. Table 2 gives an overview of the uncertainty values, showing that σ_{d_i} is the lowest with a value of 0.24 pixels, for the *Zeiss* lens. The diameter uncertainty is one order of magnitude larger for the *Questar* configurations, reaching up to almost 11 pixels. Intuitively, given the better defocusing sensitivity at larger magnifications, one might come to the simple suggestion that the particle z location is still better, even if the particle-image diameter uncertainty is larger. However, it becomes apparent that using the *Zeiss* lens is beneficial not only for measuring a larger FOV, but also concerning the particle z-location determination. Furthermore, σ_z is 3 times lower as compared to the *Questar* $M = 5.2$ and $M = 7.6$ configurations. The uncertainty is almost 6 times lower as for the $M = 15$ configuration.

In relation to the measurement depth of around 1500 µm, the uncertainty of the particle z location yields only 1.1% for the *Zeiss* lens.

Table 2. For the different optical configurations: the uncertainty of the particle-image diameter determination, $2\sigma_{d_i}$, and the related uncertainty of the particle z location determination, $2\sigma_z$.

configuration	M [-]	$2\sigma_{d_i}$ [pixel]	$2\sigma_z$ [µm]
● *Zeiss* 50 mm	0.8	0.24	16.4
● *Questar* + 2×	5.2	2.12	49.6
● *Questar* + 3×	7.6	3.12	48.4
● *Questar* + 6×	15	10.98	98.8

The lower performance of the *Questar QM 1* optics has a variety of reasons. One is that the minimum working distance of around 560 mm is relatively large: compared to a microscope objectives with a small working distance of less than 10 mm used in Fuchs & Kähler (2019), at a similar magnification (13 vs. 15, here), the defocusing sensitivity was $s^Z = 2.05$ µm/pixel, whereas here a value of only 9.0 was achieved. Moreover, the optical characteristics of the *Questar* lead to particle image shapes where the defocused ring is spread out over around 20 pixels combined with a very noisy intensity distribution that barely exceeds the background intensity (see Fig. 3 for the examples of the intensity distribution). In terms of the SNR this results in a significant detriment relative to the *Zeiss* lens, since for the latter, the defocused ring has a width of around 3 pixels with a very distinct intensity distribution. These conditions are perfect for determining the edge location of the particle images with high accuracy. Comparing the σ_{d_i} values achieved in this experiment using the *Zeiss* lens against what was found by Fuchs et al. (2016), it becomes apparent that the uncertainty here is significantly lower, ~ 0.25 pixel vs. ~ 1 pixel before, even though the optical configuration was similar. However, in the current experiment seeding particles with a diameter of 10 µm were used in a liquid flow, whereas in the previous study an air flow using DEHS particles with a diameter of around 0.35 µm was used. As a result the SNR was lower and so is the accuracy of the diameter estimation, which is also observed when comparing the *Questar* configurations with the *Zeiss* configuration in the present study.

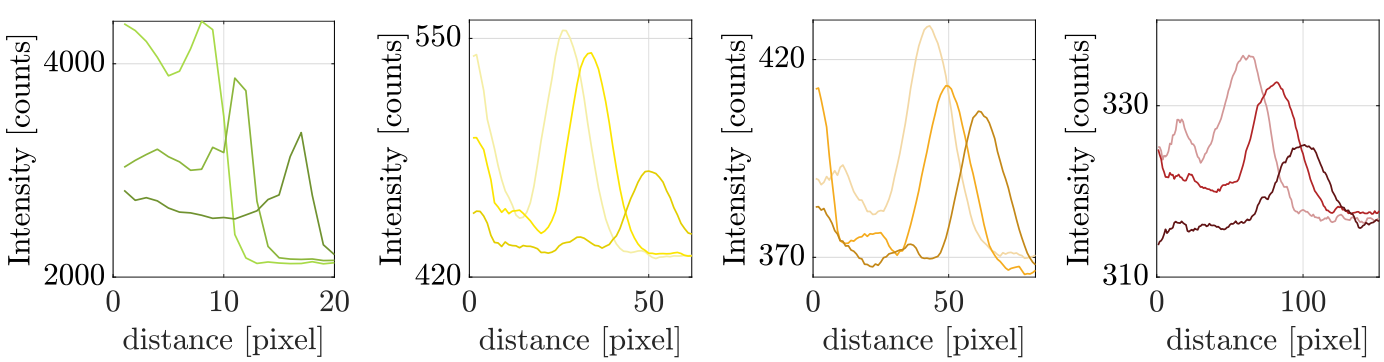

(a) ●$M = 0.8$; (b) ●$M = 5.2$; (c) ●$M = 7.6$; (d) ●$M = 15$;

Figure 3. Radial intensity distribution of three exemplary particle images for each magnification.

3.2. Fluid mechanic outcomes

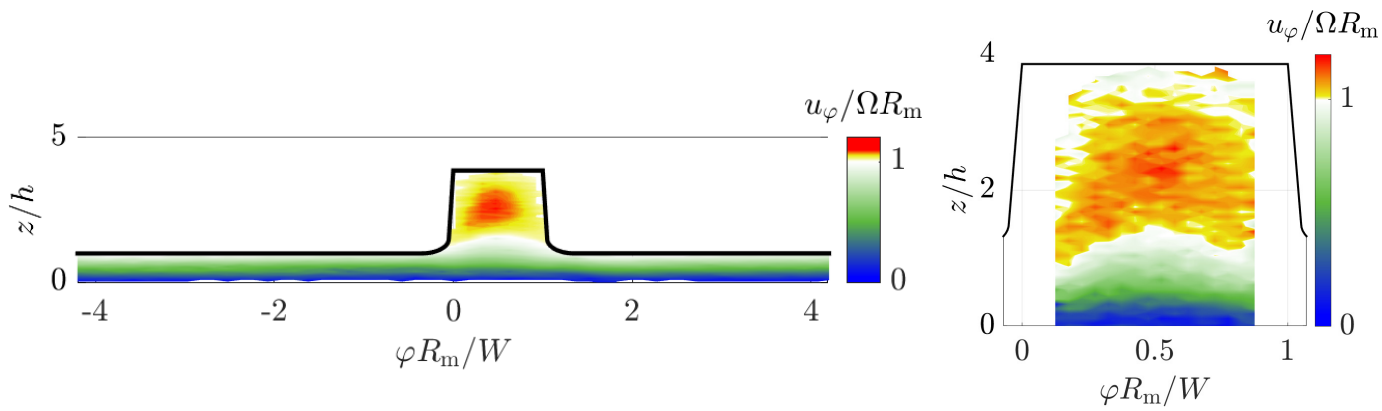

(a) circumferential velocity at •$M = 0.8$;

(b) circumferential velocity at •$M = 15$

Figure 4. Distribution along z and φ of normalized u_φ for the extreme cases of the magnifications at $R = R_\mathrm{m}$. The origin of $\varphi R_\mathrm{m}/W$ is set to the left edge of the groove.

The previous sections focused on the accuracy of each magnification, while the present section takes the fluid mechanic results into consideration. The smallest magnification enables an investigation into groove-to-groove interactions. This is important knowledge in terms of an applicability for clutch manufacturers, since this part up-to-now could only be reached with numerical efforts. A considerably wide FOV, with an accuracy, that is sufficient to depict the most important fluid mechanic phenomena, is beneficial for this flow scenario.

The largest magnification displays only a fracture of the groove, thus the particles have a significant lower intensity as shown in Figure 3 compared to the particles of the smallest magnification. This partially explains the location uncertainty discussion as outlined in Section 3.1. Figure 4 shows the circumferential velocity distribution along the z and φ-space coordinate as normalized presentment. The velocity is normalizes with the locally found disk velocity ΩR_m, while the spatial coordinates are scaled with the gap height h and the groove with W, respectively. The origin of ordinates is located on the left side of the groove at the glass plate. Both magnifications depict the ongoing fluid mechanic phenomena appropriately. While for the most part of the smooth gap a Couette-like flow is present, this fact changes in the vicinity of the groove. An engineering guideline for a quantification is the region of $\varphi R_\mathrm{m}/W \in [-1; 2]$, where the flow deviates significantly from the ideal analytical solution as outlined in e.g. Leister, Najafi, et al. (2021). The slightly higher velocity compared to the disk velocity ΩR_m in the rear part of the groove (indicated with a yellow-to-red color distribution) is part of the intra-groove vortex as discovered and outlined by Leister, Fuchs, et al. (2021). Both magnifications are able to depict this eminently important fluid phenomenon accordingly.

Figure 5 shows the circumferential velocity in the middle of the groove at $\varphi R_\mathrm{m}/W = 0.5$ for all FOVs. To enable a fair comparison between all set-ups the same amount of particles were used (≈ 500). The z-values were divided in 100 µm divisions. Additionally, the standard deviation σ_{u_φ} is shown for each magnification and z-bin. As already indicated earlier in Section 3.1, the trend of

a lower uncertainty for the smallest magnification is not only visible for the spatial consideration, but also within the velocity data. The highest magnification yields the largest velocity uncertainty. The reason being similar to the already discussed spatial accuracy. The standard deviation in the gap region is mainly introduced to the higher velocity gradient and a finite fragmentation of the z-binning. For the largest magnification additionally some outliers at low z-coordinates make a noticeable influence. Note, that the error is relatively constant within the groove. Only for the highest magnification a slight increase at the largest z/h-values is visible, which indicates a too low SNR at this part for this specific parameter combination.

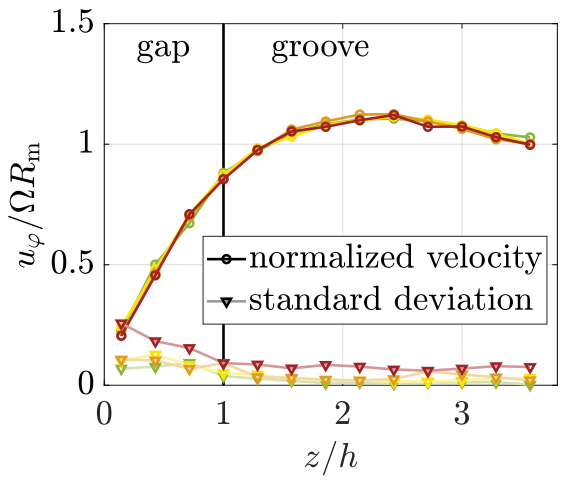

Figure 5. Comparison of the circumferential velocity u_φ and the standard deviation σ_{u_φ} at $\varphi R_\mathrm{m}/W = 0.5$ along z for all magnifications (●$M = 0.8$; ●$M = 5.2$; ●$M = 7.6$; ●$M = 15$).

4. Conclusions

With this experimental open wet clutch flow investigation a large magnification range from macroscopic to microscopic consideration was successfully conducted. It was possible to show, that all four magnification levels were able to depict the fluid flow and the ongoing phenomena in an open wet clutch. Furthermore, defocusing PTV offers its unrestricted suitability for such a flow scenario. Defocused particles with only around 10 counts difference to the background were successfully detected for the largest magnification. It has be shown that, for defocusing PTV, larger magnifications do not necessarily yield a higher accuracy in the particle z location determination, along the optical axis. In fact, using a *Zeiss* macro objective lens at $M = 0.8$ outperformed a *Questar QM1* long-distance microscope ($M = 5 - 15$, depending on the configuration) by at least a factor of 3 in terms of the particle z location uncertainty. As a result of the larger minimum working distance and the inferior imaging quality of the *Questar*, the signal-to-noise ratio of the particle images was significantly lower as in the case of the *Zeiss* lens, leading to a significantly higher uncertainty of the particle-image diameter determination. However, simply using standard microscope objectives instead of the long-distance microscope lenses is not feasible for several reasons: First, the geometric and assembly constraints do not allow for placing imaging lenses close to the

clutch. Second, the measurement depth of more than 1 mm would yield particle image sizes of several hundred pixels due to the large defocusing sensitivity. As a result the seeding concentration would have to be low and the low SNR of these very large particle images would make the particle location determination inaccurate with distance to the focal plane. Third, illuminating and at the same time imaging the volume would require a complex optical configuration, since the lens would block the angled illumination of the volume. Altogether, it showed that the *Zeiss* lens had the best accuracy, while at the same time being able to capture a large field of view, allowing for a comprehensive investigation of the clutch flow.

For future defocusing PTV experiments it seems appropriate to not only consider the defocusing sensitivity as decisive factor, but also take the intensity and the corresponding gradients into account. Analog findings have been made for the fluid mechanic outcomes. All four magnification levels were able to depict the gap flow and the ongoing vortex phenomena in the groove. For a quantitative comparison along the z coordinate the fluid flow in the middle of the groove was chosen. The velocity uncertainty increases with increasing magnification. However, the increase of velocity uncertainty along z for larger magnifications wasn't as strong as the afore-elaborated z-location uncertainty increase. This can be traced back to the fact, that the entire measurement depth was considered, instead only the part near the stator.

The demand of a FOV, which spans the region between the inner and the outer radius as well as an intra-groove consideration with a much smaller FOV has been met with this technique. The tested approach of defocusing particle tracking velocimetry is thus considered particularly suitable for such industry-based flow scenarios and appears qualified for further investigations of the flow in an open wet clutch across the board of utilized groove geometries.

References

Fuchs, T., Hain, R., & Kähler, C. J. (2016). In situ calibrated defocusing ptv for wall-bounded measurement volumes. *Measurement Science and Technology*, *27*(8), 084005. Retrieved from https://doi.org/10.1088/0957-0233/27/8/084005

Fuchs, T., & Kähler, C. J. (2019). Single axis volumetric µPTV for wall shear stress estimation. In C. J. Kähler, R. Hain, S. Scharnowski, & T. Fuchs (Eds.), *Proceedings of the 13th international symposium on particle image velocimetry.* Retrieved from https://athene-forschung.unibw.de/doc/129386/129386.pdf

Grötsch, D., Niedenthal, R., Völkel, K., Pflaum, H., & Stahl, K. (2019). Effiziente CFD-Simulationen zur Berechnung des Schleppmoments nasslaufender Lamellenkupplungen im Abgleich mit Prüfstandmessungen. *Forschung im Ingenieurwesen*, *83*, 227-237. Retrieved from https://doi.org/10.1007/s10010-019-00302-3

Leister, R., Fuchs, T., Mattern, P., & Kriegseis, J. (2021). Flow-structure identification in a radially grooved open wet clutch by means of defocusing particle tracking velocimetry. *Experiments in*

Fluids, *62*(2), Article: 29. Retrieved from https://doi.org/10.1007/s00348-020-03116-0

Leister, R., Najafi, A. F., Kriegseis, J., Frohnapfel, B., & Gatti, D. (2021). Analytical modeling and dimensionless characteristics of open wet clutches in consideration of gravity. *Forschung im Ingenieurwesen*, *85*(4), 849–857. Retrieved from https://doi.org/10.1007/s10010-021-00545-z

Neupert, T., Benke, E., & Bartel, D. (2018). Parameter study on the influence of a radial groove design on the drag torque of wet clutch discs in comparison with analytical models. *Tribology International*, *119*, 809–821. Retrieved from https://doi.org/10.1016/j.triboint.2017.12.005

Olsen, M. G., & Adrian, R. J. (2000). Out-of-focus effects on particle image visibility and correlation in microscopic particle image velocimetry. *Experiments in Fluids*, *29*(7), S166–S174. Retrieved from https://doi.org/10.1007/s003480070018

Willert, C. E., & Gharib, M. (1992). Three-dimensional particle imaging with a single camera. *Experiments in Fluids*, *12*(6), 353–358. Retrieved from https://doi.org/10.1007/BF00193880